

Electron transfer and emission in slow collisions of N^{5+} with C_{60}

Uwe Thumm

Department of Physics, Kansas State University, Manhattan, KS 66506-2601, USA

Received 31 August 1994

Abstract. Within a semiclassical overbarrier model for non-destructive, long-range charge exchange, the population dynamics of target and projectile levels, charge-state evolution and electron emission during the scattering of 50 keV N^{5+} ions on C_{60} are simulated. The model describes the transient formation of hollow projectiles due to resonant electron capture and Auger relaxation of the multiply excited projectiles. Estimates for total cross sections in charge-state-changing collisions and the deflection functions for the dynamical Coulomb trajectory are given. Evidence for a strong enhancement of the angle-differential scattering cross section is found and related to the dielectric response of the target.

1. Introduction

Collisions of highly charged ions (HCI) with C_{60} are currently attracting increasing interest (Walch *et al* 1994, LeBrun *et al* 1994, Scheier and Märk 1994). The experiments performed by Walch *et al* (1994) probed the interaction between slow HCIs and gaseous C_{60} targets and measured the final charge states of target and projectile in coincidence. This coincidence measurement allowed for the distinction between hard collisions at relatively small impact parameters that lead to fragmentation of the target-carbon cage, and non-destructive, soft collisions at larger impact parameters. The complicated multifragmentation has been described by a bond-percolation model (LeBrun *et al* 1994) that is closely related to a nuclear fragmentation model (Bauer 1988) used to simulate (Hirsch *et al* 1984) the fragmentation of heavy nuclei by fast proton impact. For non-destructive collisions with C_{60} , a semiclassical overbarrier model (OBM) has recently been developed (Thumm 1994†, hereafter to be referred to as I). This model allows for the simulation of the occupation dynamics in projectile and target levels, charge-state evolutions, and the emission of Auger electrons during the collisions. First numerical applications of the OBM to 80 keV Ar^{8+} ions colliding with C_{60} are in reasonable agreement with experiment (see I).

In this work, the results of a similar OBM calculation for the scattering of slow (50 keV) N^{5+} ions on C_{60} in non-destructive, charge-state-changing collisions are presented. The model predictions may provide guidelines for planned experiments (Schulze and Salzborn 1994). A detailed description of the OBM applied to HCI- C_{60} collisions is given in I, and only its key features will be summarized in section 2. Numerical results and their discussion follow in section 3. Finally, a brief summary and conclusions are contained in section 4. Atomic units are used unless otherwise stated.

† In this reference, a factor 1/2 is missing in the nuclear and electronic self-image potentials. However, the results shown in this reference are not sensitive to the self-image potentials. For the present work this factor 1/2 was included and is of relevance, since the nuclear self-image potential affects the deflection function (cf section 3.4).

2. Theory

The electronic structure of C_{60} is modelled on the basis of levels m of energy ϵ_m^t , degeneracies B_m and occupations b_m calculated within the one-electron spherical-shell model of Puska and Nieminen (1993). Within this model, the target has 240 delocalized valence electrons that occupy the 15 lowest energy levels in a self-consistently determined effective potential ranging from the bottom of the valence band at $\epsilon_1^t = -33.7$ eV to the highest occupied level, the Fermi level, at $\epsilon_{15}^t = -7.44$ eV. All levels below ϵ_{15}^t are fully occupied, level $m = 15$ is partially occupied with $b_{15} = 28$ electrons, and levels above ϵ_{15}^t are empty. The remaining 120 electrons of C_{60} occupy core levels localized near individual carbon nuclei of the cluster. During the interaction with the projectile, energy levels and occupations change as a function of R , the 'internuclear' distance between the target centre-of-mass and the projectile. At finite R , the target energy levels $\epsilon_m^t(R)$ are shifted downward in the electric field of the projectile. Furthermore, after the capture of target electrons, positive charge accumulates on the target, which results in an additional downward shift of the target spectrum.

The projectile is described within an independent electron approach based on hydrogenic shells n with energy levels, occupations numbers and degeneracies denoted by $\epsilon_n^p(R)$, $a_n(R)$, and $A_n = 2n^2$. Sublevels are not resolved and no angular momentum quantum numbers are assigned. During the interaction with the target, the energetic positions of the projectile levels change due to image charge effects, a possibly charged target and the dynamical change in screening induced by varying level populations.

According to the classical OBM for charge transfer, the active electron is required to overcome the potential barrier between target and projectile that is formed by the the total potential

$$V(q, Q, R, z) = -\frac{q}{|R-z|} - \frac{Q}{z} + V_{\text{im}}(q, R, z) \quad (1)$$

where q and Q are the total charges of projectile and target acting on the electron in transition, and where a different sign convention from that in I has been used. The electron coordinate along the 'internuclear axis' is denoted by z . The image potential V_{im} includes the active electron's self image and the nuclear image. Location and height of the potential barrier are determined by the maximum of (1) and can be approximated by

$$z_B(q, Q, R) \approx \begin{cases} \max\{R(1 + \sqrt{q/Q}), a + \Delta a/2\} & \text{if } Q \neq 0 \\ a + \Delta a/2 & \text{if } Q = 0 \end{cases}$$

and

$$V_B(q, Q, R) \approx -R^{-1}(Q + q + 2\sqrt{qQ}) \quad (2)$$

where $a = 6.7$ and $\Delta a = 5.6$ are the radius and thickness of the spherical shell.

During the motion of the projectile, energy levels, the conditions for charge exchange (in particular transition rates, and total and effective charges of target and projectile), vary as a function of R . The time evolution of occupation numbers for projectile and target levels, the emitted electron yield and the centre-of-mass motion of the projectile are obtained as the solution of a set of (highly non-linear) coupled classical rate equations.

The semiclassical model pictures resonant charge exchange as the classical motion of the active electron from an initial quantum state to a final quantum state. Quantum aspects

are contained in the discrete nature of the energy levels and the modelling of the transition rates. In an adiabatic approximation, it can be assumed that electronic transitions are so fast that practically R does not change during the transition time. Analytical expressions for the transition rates for resonant electron capture, Γ_{RN} , resonant electron loss, Γ_{RL} and Auger transition rates are derived in I.

As the projectile approaches the target, the first resonant transfer of an electron becomes possible when the potential barrier V_B energetically moves below the highest occupied target level, $\epsilon_{15}^t(R)$. The distance, R_1^* , at which this may happen, is obtained numerically from the condition

$$\epsilon_{15}^{(i)}(R_1^*) = V_B(q, Q, R_1^*)$$

where $q = q^p(t = -\infty)$ and $Q = 1$. The generalization of this condition leads to decreasing critical radii $R_1^* > R_2^* > R_3^* \dots$ for the sequential capture of electrons on the incoming trajectory. An approximate expression for R_1^* , obtained analytically by using (2), is

$$R_1^* \approx \frac{1 + 2\sqrt{q^p(t = -\infty)}}{|\epsilon_{15}^t(t = -\infty)|}. \quad (3)$$

From the known initial occupations of target and projectile at time t_0 , a_n^0 and b_m^0 , the occupation numbers, a_n and b_m , at any time $t > t_0$ are obtained by integrating a set of rate equations of the form

$$\frac{d}{dt}a_n = \Gamma_{RN} - \Gamma_{RL}a_n + \sum_{n' > n} \Gamma_{n',n} - 2 \sum_{n' < n} \Gamma_{n,n'} \quad (4)$$

$$\frac{d}{dt}b_m = \Gamma_{RL} - \Gamma_{RN}. \quad (5)$$

In order to simplify the notation, statistical weights are included in the transition rates, in contrast to the more explicit notation of I. Since all rates Γ and occupation numbers implicitly depend on $R(t)$, the above equations have to be solved simultaneously with Newton's equation for the projectile motion. With respect to Auger processes, only transitions for which the two active electrons start in the same shell are explicitly included. These fast transitions partially relax the multiply excited projectile while competing resonant electron transfer occurs (I, Burgdörfer *et al* 1991). The corresponding rates are denoted by Γ_{n_i, n_f} , where n_i and n_f relate to the initial and final shell. Slow Auger relaxation channels are not included and can be neglected *during* the collision, i.e. while resonant electron transfer takes place. Further downstream, however, when resonant transfer processes are classically forbidden, slow Auger processes may decisively influence the final charge state of a highly charged projectile. For the moderately charged projectile studied in this paper, a few slow Auger and radiative relaxation steps can be accounted for by enhancing our dynamical simulation with a simple relaxation scheme (cf Ali *et al* 1994).

Within the independent electron picture, the energy of an Auger electron emitted at time t from level n_i , while a second projectile electron transfers from n_i to a lower level n_f , is given by

$$\epsilon_A(t) = 2\epsilon_{n_i}^p(R(t)) - \epsilon_{n_f}^p(R(t)).$$

Collecting the emitted Auger electrons in energy bins $[\epsilon_k] \equiv [(k-1)\Delta\epsilon, k\Delta\epsilon]$, $k = 1, 2, \dots$, with widths $\Delta\epsilon$ of the order of the experimental energy resolution, a set of rate equations for

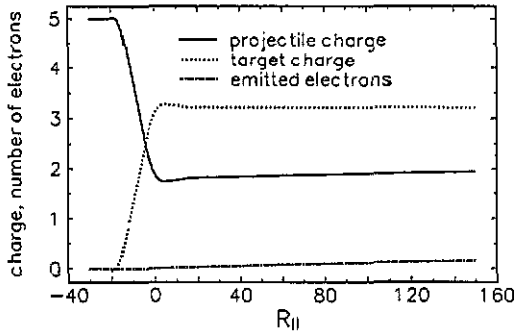


Figure 1. Charge-state evolution and Auger electron emission for 50 keV N^{5+} ions colliding with C_{60} with impact parameter $b = 13$. The distance R_{\parallel} is the projection of the target-projectile distance onto the incident-beam direction; at the point of closest approach $R_{\parallel} = 0$.

the numbers $c_k(t)$ of electrons emitted in each energy bin before time t can be formulated (statistical weights are included in the transition rates, cf (I)),

$$\frac{d}{dt}c_k = \sum_{n_f} \sum_{n_i > n_f} \Gamma_{n_i, n_f} \times \begin{cases} 1 & \text{if } \epsilon_A(t) \in [\epsilon_k] \\ 0 & \text{otherwise.} \end{cases}$$

At large R and before overbarrier charge exchange becomes possible, the projectile is merely slightly attracted by the image potential it induces in the target. In addition, as R decreases below the critical value for the onset of electron capture, R_1^* , the projectile motion is also influenced by the repulsive Coulomb interaction between both, now positively charged, collision partners and continues to move on a dynamic Coulomb trajectory.

3. Numerical results and discussion

In the following subsections, the dynamical change in charge states, occupation numbers and electron emission for a *fixed* impact parameter b will be discussed first. Then results for charge states, level occupations, energy-differential electron yields, and the deflection of the projectile after the collision will be presented as a function of b . In all calculations, full screening by inner and no screening by outer projectile electrons was assumed.

3.1. Evolution of charge states, occupations and electron emission

This subsection contains numerical results for the fixed impact parameter $b = 13$ and the projectile velocity $v = 0.378$, corresponding to 50 keV N^{5+} ions, addressed in an experiment proposed by Schulze and Salzborn (1994). Figure 1 shows the evolution of projectile and target charge states, as well as the number of emitted projectile Auger electrons during the collision. The distance R_{\parallel} on the abscissa is the projection of the projectile-target distance R on the direction of the incoming projectile. Thus, for the incoming trajectory $R_{\parallel} < 0$, for the outgoing trajectory $R_{\parallel} > 0$, and $R_{\parallel} = 0$ at the point of closest approach. As the projectile approaches the C_{60} cluster, charge exchange starts at the critical distance $R_{\parallel} = (R_1^{*2} - b^2)^{1/2}$ where $R_1^* \approx 22$. Subsequently, the projectile captures additional electrons and reaches its lowest charge state near the point of closest approach on the outgoing trajectory. Shortly thereafter resonant charge exchange stops, and the target charge remains unchanged while the projectile charge increases due to Auger relaxation.

A more detailed picture of the neutralization dynamics is given in figure 2, where changes in occupation numbers (i.e. the instantaneous occupation, $a_n(t)$ or $b_m(t)$, minus the initial occupation, a_n^0 or b_m^0 , of a particular projectile or target level) are shown as a function of R_{\parallel} , including all projectile levels n (figure 2(a)) and target levels m (figure 2(b)) that are coupled. With respect to the target (figure 2(b)), the highest occupied level $m = 15$ participates by far the most actively in the charge-exchange process and loses three electrons to the incoming projectile. Some resonant loss to the highest target levels occurs but remains insignificant. With respect to the projectile (figure 2(a)), levels $n = 4$ and 5 get resonantly fed by target level $m = 15$ on the incoming trajectory. Auger relaxation of the projectile on the outgoing trajectory slightly depletes levels $n = 4$ and 5 and results in a very small electron flux into level $n = 2$. In the shown R_{\parallel} interval, this depletion is not completed and, at $R_{\parallel} = 150$, the projectile keeps electrons in highly excited states (mainly in $n = 4$). It continues to relax by emitting electrons as it moves further away from the target. The maximum in the population for projectile level $n = 5$ is due to partial resonant neutralization followed by resonant ionization into target levels $m = 17 \dots 20$ at small R_{\parallel} on the incoming trajectory.

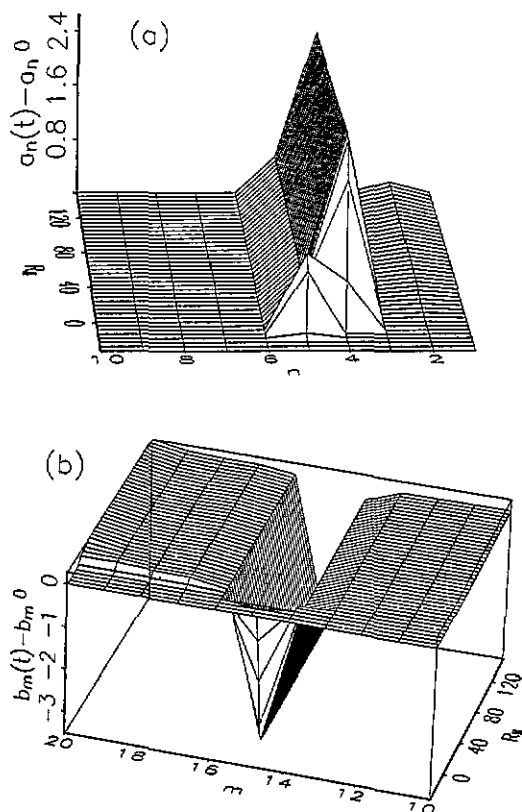


Figure 2. Evolution of the changes in projectile (a) and target (b) occupation numbers during the collision. Collision system and parameters as in figure 1. Projectile states are labelled by n , target states by m .

The time-dependent emission of Auger electrons is shown in figure 3, where the Auger yield, differential in energy, is plotted against R_{\parallel} and the energy of the emitted electron.

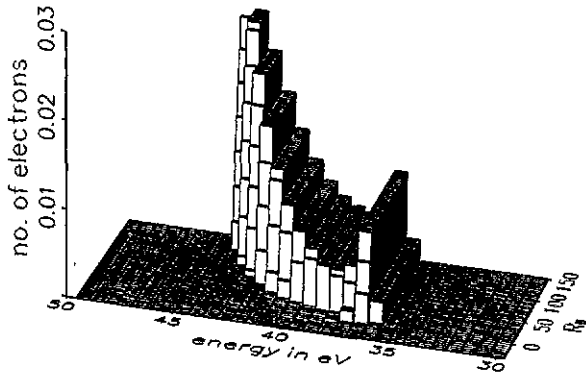


Figure 3. Emission of projectile Auger electrons during the collision into energy bins of width 0.67 eV. Collision system and parameters as in the previous figures.

The emitted electrons are collected in energy bins of width 0.67 eV. The displayed electron yield is normalized to a single projectile. All emitted electrons are due to Auger transitions that populate level $n = 2$ while depopulating level $n = 4$. The slowest electrons are emitted first and the most energetic electrons are emitted at larger distances from the target. Even though level $n = 5$ gets resonantly filled (cf figure 2(a)), our simulation predicts its depletion by resonant loss and not by Auger transitions.

3.2. Impact-parameter dependence of charge states, occupation numbers and Auger spectra

Figure 4 shows the final charge states of projectile and target, together with the number of emitted Auger electrons. With respect to the Auger transitions considered in this simulation, all results in this and subsequent subsections include the downstream Auger relaxation for $R_{||} > 150$, i.e. beyond the range of distances $R_{||}$ shown in the previous figures. Within our classical model, no electronic interaction is possible if the projectile trajectory does not intersect with a sphere of radius R_1^* around the target, and no charge exchange occurs for impact parameters larger than about 22. Auger electrons are emitted for not too distant collisions with $b < 15$. The reason for this restriction of Auger emission to values of b that are clearly smaller than R_1^* is that Auger transitions only occur after excited levels have received at least two electrons. This feature is recognized in figure 5(a), where the occupations of the lowest shown projectile levels increase for $b < 15$. For slightly more distant collisions ($15 < b < R_1^*$) resonant charge exchange still occurs, however, no emission of Auger electrons is predicted. With respect to the target (figure 5(b)), level $m = 15$ is most active at all impact parameters. Resonant loss into levels $17 \leq m \leq 20$ occurs at smaller impact parameters, but is comparatively very small. The extrema in figure 4 at $b = 13$ are artifacts of our model that opens and closes resonant and Auger transition channels as energy levels get shifted and occupations change, thereby allowing for non-integer occupation and charges.

For incident 80 keV Ar^{8+} there is experimental evidence that the C_{60} cage is destroyed in close collisions with impact parameters $b < 14$ (Walch *et al* 1994). In contrast, for 50 keV N^{5+} projectiles, our simulation predicts a different scenario. At impact parameters $b > 10$ the predicted target charge states remain distinctively smaller than charge states ($q^t > 6$) that lead to unstable cluster ions. Fragmentation due to multiple ionization does not occur for projectile trajectories that do not intersect the cluster in very close collisions with $b \leq a + \Delta a = 9.5$. This leads to the following picture. Fragmentation due to

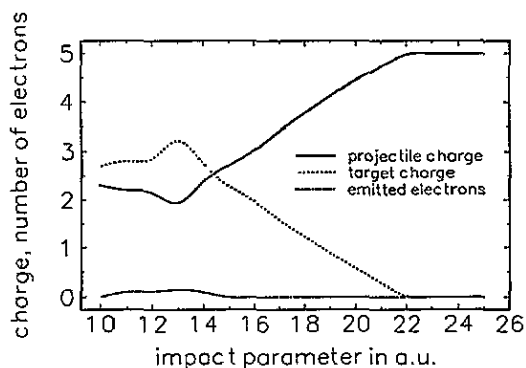


Figure 4. Final charge states and numbers of emitted Auger electrons for 50 keV N^{5+} ions colliding with C_{60} as a function of the impact parameter.

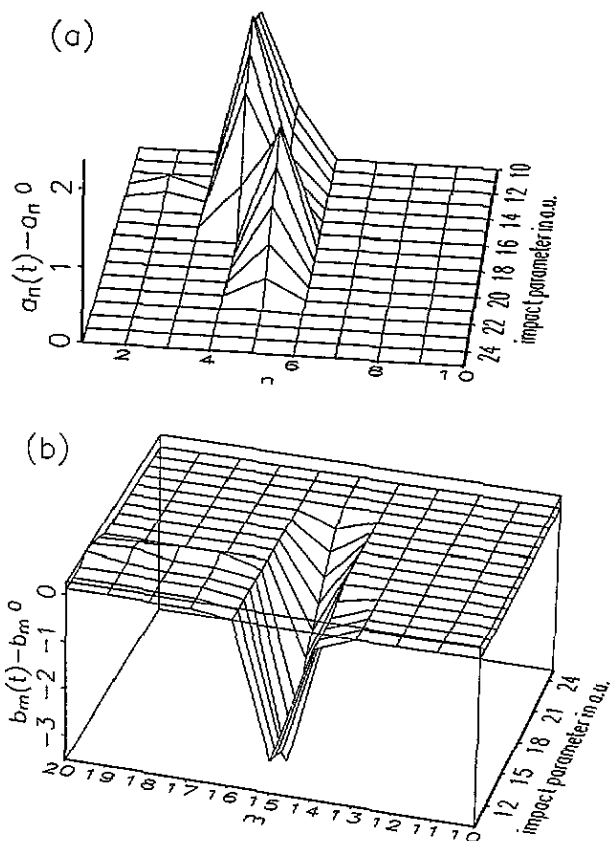


Figure 5. Final occupation changes in projectile levels n (a) and target levels m (b) as a function of the impact parameter. System and parameters as in figure 4.

multiple ionization requires highly charged projectiles; for moderately charged projectiles (such as N^{5+}) fragmentation may only result due to a different mechanism, e.g. the energy

transfer to individual carbon atoms in very close collisions, in which the projectile trajectory nearly 'touches' or intersects the cluster. Therefore, focusing on non-destructive collisions with 50 keV N^{5+} projectiles, a reasonable estimate for the minimal impact parameter for non-destructive, collisions is $b_{\min} = 10$, which is of the order of $a + \Delta a$. Then for all impact parameters, less than three electrons remain in excited projectile states after the projectile has relaxed with regard to the fast Auger transitions included in this simulation. Therefore, it may be assumed that downstream Auger relaxation, due to transitions not yet included in the results in figure 5(a), leads to the emission of, at most, two additional projectile electrons before the Auger relaxation sequence is completed. Thereafter, projectile relaxation might continue by, in general, much slower radiative transitions. Comparison with figure 4 now leads to the prediction of fully relaxed projectiles, which, after charge-state changing collisions, hit the detector in the final charge states 3+ and 4+. A similar estimation of the effect of slow Auger relaxation channels for the case of 80 keV Ar^{8+} lead to reasonable agreement with experiment (see I).

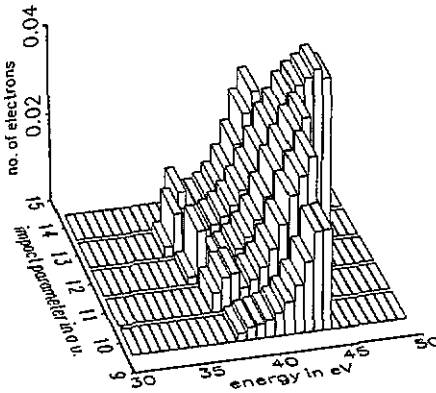


Figure 6. Projectile Auger electron yield as a function of impact parameter and emitted electron energy. The energy bins have a width of 0.67 eV. System and parameters as in figure 5.

The spectrum of emitted Auger electrons, i.e. the numbers c_k of electrons emitted in particular energy bins and resulting from fast Auger transitions, as a function of b is presented in figure 6. Figure 7 shows the energy-differential Auger yield, y_k , after integration over impact parameters between b_{\min} and R_1^* ,

$$y_k = \frac{2\pi}{A} \int_{b_{\min}}^{R_1^*} db b c_k(b). \quad (6)$$

y_k is normalized to the area A perpendicular to the incident beam direction that is run through by projectiles on charge-state-changing trajectories:

$$A = \pi(R_1^{*2} - b_{\min}^2). \quad (7)$$

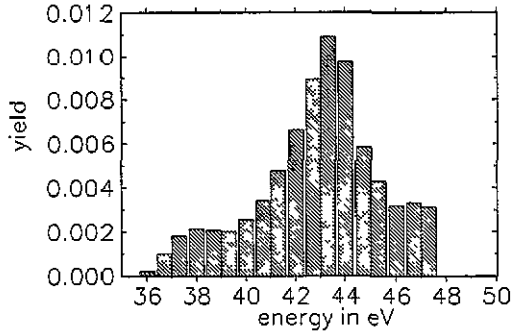


Figure 7. Projectile Auger electron yield of figure 6, integrated over impact parameter and normalized according to equations (6) and (7).

3.3. Cross sections

The critical distances R_i^* for sequential overbarrier capture are related to geometrical cross sections for the production of specific charge states, $+i$, of C_{60} by

$$\sigma_i = \pi(R_i^{*2} - R_{i+1}^{*2}) \quad (8)$$

and to the total geometrical cross section for charge exchange in non-destructive collisions by $\sigma_{\text{tot}} = \pi R_1^{*2}$. Theoretical estimates for the critical overbarrier distances can be extracted from the impact-parameter-dependent final charge states of the target in figure 4. Table 1 shows the radii R_i^* and corresponding cross sections. The total cross section amounts to $\sigma_{\text{tot}} = 4.3 \times 10^{-14} \text{ cm}^2$ and is smaller than the calculated total cross section ($6.2 \times 10^{-14} \text{ cm}^2$) for Ar^{8+} projectiles (see I).

Table 1. Critical overbarrier radii R_i^* and cross sections σ_i for the production of final target charge states $+i$ for electron capture in 50 keV N^{5+} on C_{60} collisions.

i	R_i^* (au)	σ_i (10^{-15} cm^2)
1	22.1	20.4
2	16.0	6.3
3	13.6	—

3.4. Deflection function and dielectric response

Figure 8 displays the deflection function, i.e. the projectile scattering angle as a function of impact parameter, for two incident projectile velocities, $v = 0.378$ (corresponding to 50 keV nitrogen ions, figure 8(a)) and $v = 0.0378$ (corresponding to 500 eV, figure 8(b)). For the underlying trajectory calculation, the instantaneous charges of target and projectile are rounded to nearest integer values, which accounts for the step-like structures. Subbarrier tunnelling transitions, which are not included in this simulation, tend to smear out these structures. In order to determine the influence of the target dielectric response on the

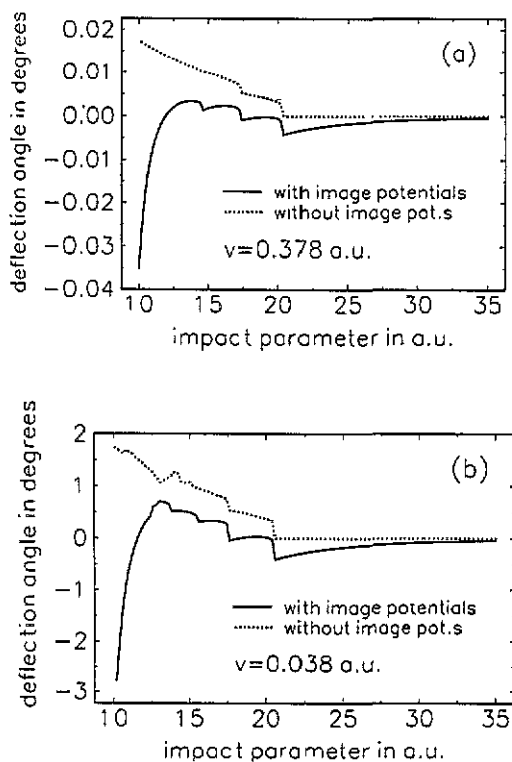


Figure 8. Deflection function for 50 keV (a) and 500 eV (b) N^{5+} ions. For the dotted curves the image potentials have been 'turned off'.

projectile deflection, a separate simulation was performed, in which the image potentials were 'turned off' in both the trajectory calculation itself and the projectile level shifts.

As one might expect, the results in figures 8(a) and (b) are qualitatively similar, with an order of magnitude larger deflection for the ten times smaller impact velocity. At impact parameters larger than the critical radius R_1^* , the full simulation (full curves) includes the deflection of the projectile in the attractive image potential. For the same impact-parameter range and 'turned off' image potentials, the projectile moves on a straight line (dotted curves). As the impact parameter is decreased below R_1^* , the target starts accumulating positive charge, which tends to repel the projectile. For impact parameters between ~ 12 and $\sim R_1^*$, this repulsive scattering is stronger than the influence of the image potentials, resulting in positive scattering angles. Interestingly, as the impact parameter is further decreased, the dielectric response again starts to dominate the deflection, and the scattering angle becomes again negative. However, for these close distances, the concept of a static asymptotic image potential is questionable, and our results at, say, $b < 12$ have to be taken with a grain of salt.

In their overall trend the deflection functions for the full simulation (full curves in figure 8) appear to have a broad maximum. The corresponding zero derivative in the deflection function is expected to produce a strong enhancement in the measured angle-differential scattering cross section, corresponding to a 'rainbow-scattering' maximum. For the lower of the shown velocities, an experimental angle resolution of $\sim 0.01^\circ$ (Walch and

Cocke 1994) points to a possibly measurable prominent structure in the angle-differential cross section that is created by the competition of repulsive dynamic Coulomb scattering and attractive dynamical-response effects.

4. Summary and conclusions

The classical OBM for ion-cluster collisions developed in I has been applied to slow collisions between a moderately charged nitrogen ion and C_{60} in order to predict the dynamics of charge transfer and electron emission in non-destructive collisions. The results for the occupation dynamics of target and projectile levels illustrate the dynamical flow of electrons to and from particular levels. The evolution of occupation numbers of target and projectile levels together with the projectile Auger electron emission, as well as final-charge-state distributions and energy-resolved Auger spectra, have been estimated and discussed.

The geometrical cross sections for the production of particular target charge states and the total cross section for non-destructive, charge-state-changing collisions were derived from the simulated charged-state distribution. As expected, the cross section for incident N^{5+} ions are smaller than for slow Ar^{8+} projectiles studied in I. In addition, it appears that for N^{5+} resonant capture of delocalized electrons does not lead to fragmentation of C_{60} , in sharp contrast to experimental (Walch *et al* 1994) and theoretical (I) evidence for 80 keV Ar^{8+} impact. Thus fragmentation due to resonant charge exchange appears to require a minimal interaction strength that is not reached for N^{5+} ions at 50 keV impact energy. The deflection function has been calculated and analysed in view of its dependence on the target dielectric response. For very slow projectile ions, the dielectronic response of the delocalized target electrons might leave a measurable signature in the projectile deflection and lead to a large enhancement of the angle-differential scattering cross section, known as 'rainbow scattering'. Experiments that might probe this effect are currently in progress (Walch and Cocke 1994). Relevant experimental data might soon become available and facilitate refinement and tests of this simulation.

Acknowledgments

Stimulating discussions with C L Cocke, E Salzbom, R Schulze, and B Walch are gratefully acknowledged. This work was supported by the Division of Chemical Sciences, Basis Energy Sciences, Office of Energy Research, US Department of Energy.

References

- Ali R, Cocke C L, Raphaelian M L A and Stöckli M 1994 *Phys. Rev. A* **49** 3586
- Bauer W 1988 *Phys. Rev. C* **38** 1927
- Burgdörfer J, Lerner P and Meyer F W 1991 *Phys. Rev. A* **44** 5674
- Hirsch A, Bujak A, Finn J E, Gutay L J, Minich R W, Porile N T, Scharenberg R P, Stringfellow B C and Turkot F 1984 *Phys. Rev. C* **29** 508
- LeBrun T, Berry H G, Cheng S, Dunford R W, Esbensen H, Gemmell D S, Kanter E P and Bauer W 1994 *Phys. Rev. Lett.* **72** 3965
- Puska M J and Nieminen R M 1993 *Phys. Rev. A* **47** 1181
- Scheier P and Märk T D 1994 *Phys. Rev. Lett.* **73** 54
- Schulze R and Salzbom E 1994 private communication
- Thumm U 1994 *J. Phys. B: At. Mol. Opt. Phys.* **27** 3515, and references therein
- Walch B and Cocke C L 1994 private communication
- Walch B, Cocke C L, Voelpel R and Salzbom E 1994 *Phys. Rev. Lett.* **72** 1439